Optimization and Design of a Diffuse Optical Wireless Sensor Network

Thomas Kamalakis,[1,*] Zabih Ghassemlooy,[2] Stanislav Zvanovec,[3] Luis Nero Alves[4] and Mohammad Ali Khalighi[5]

[1] *Department of Informatics and Telematics, Harokopio University of Athens, Greece*
[2] *Optical Communication Research Group, Faculty of Engineering and Environment, Northumbria University, Newcastle upon Tyne, UK*
[3] *Department of Electromagnetic Field, Czech Technical University in Prague, Czech Republic*
[4] *Department of Electronics Telecommunications and Informatics, University of Aveiro and the Instituto de Telecomunicações, Aveiro, Portugal*
[5] *Aix-Marseille University, CNRS, Centrale Marseille, Institut Fresnel, Marseille, France*
[*] *thkam@hua.gr*

Abstract: Wireless sensor networks (WSNs) are currently being deployed in everyday objects to collect and transmit information related to humidity, temperature, heartbeat, motion, etc. Such networks are part of the massive machine-type communication scenario (mMTC) within the fifth/sixth generation of wireless networks. In this paper, we consider the optimization and design of an optical WSN composed of multiple battery-powered sensor nodes based on light-emitting diode transmitters. Extending our previous work, we take into account both line-of-sight and diffuse light propagation, and show that in indoor scenarios, diffuse radiation can improve link availability under shadowing/blocking and extend battery life. In order to optimize the optical wireless link parameters, we use a machine-learning approach based on a genetic algorithm to ascertain the performance limits of the system. The presented results indicate that the proposed system is a viable wireless option for WSNs within the context of mMTC.

1. Introduction

The internet-of-things (IoT) [1] constitutes one of the main drivers for the information and communication technology (ICT) industry. The fifth generation (5G) wireless networks have identified massive machine-type communications (mMTC) as a key enabler, encompassing use cases where multiple low-power sensor nodes (SNs) sporadically transmit information at relatively low data rates. Typical examples include smart-grids [2], smart cities [3], infrastructure monitoring [4], asset tracking [5], healthcare [6] and others. Wireless sensor networks (WSNs) composed of spatially distributed SNs within 5G/6G networks come with ever-increasing demands for higher energy efficiency and longer life spans [7].

WSNs offer unique features of network scalability, distributed control, etc. A range of radio frequency (RF) wireless technologies have been developed for industrial applications [8] but encounter problems such as tight wireless bandwidth resources, increased crosstalk (especially in multi-hop scenarios [9]), easy signal interception, fading, and relatively low power efficiency. Optical wireless communications (OWC) covering the infrared [10] and visible [11] part of the spectrum are being considered as part of future 5G/6G enabling technologies in certain applications, where RF-based systems are not the preferred option [12]. Typical applications include smart manufacturing [13], information proclaiming to the public [14], underwater IoT [15], intelligent transportation [16], agriculture [17] and smart health-care [18]. OWC-based WSN may offer higher data throughputs, inherent security, lower energy usage [13], [14]. However, due to the limitations of line-of-sight (LOS), energy-efficient network models and routing protocols must be used. In [19], an industrial monitoring system based on an optical camera communication system with an artificial neural network-based group detection mechanism for industry applications was proposed and implemented. In [20] and [21], channel modeling and characterization of indoor visible light communication for medical body-area networks were investigated. In [22], a triple-hop underwater WSN based on the hybrid RF and OWC links with the relay between the SNs and the access point was investigated by means of Monte-Carlo simulation. In [23], energy harvesting and energy efficient modulation schemes for visible light communication (VLC) in industrial applications were investigated.

In [24], we studied an indoor OWC-based WSN using a VLC down-link and an infrared (IR) up-link to connect master nodes (MN) and SNs. The system under consideration is shown in Figure 1. Figure 1a shows a number of SNs that are periodically sending sensor readouts to one or multiple MNs using IR OWC up-links. The MN uses a VLC down-link to send acknowledgments and coordinate transmissions. Light signals transmitted from the SN can reach the MN through the LOS path or via multiple reflections from various surfaces of the room (diffuse path). Figure 1b shows the transceiver diagram. At the transmitter (TX), the sensor information modulates the intensity of the IR LED(s) via the driver circuit. At the receiver (RX), an optical bandpass filter is used for limiting the ambient light noise prior to optical-to-electrical conversion using a PIN photodiode and a trans-impedance amplifier (TIA). In addition to the actual sensors, the node contains a micro-controller unit (MCU), which coordinates the node data transmission cycle. The MN architecture is similar except for exchanging the transmitting/receiving to use a LED-based VLC system for simultaneous communication and illumination. Considering the LOS contribution only, one may obtain significant battery lifetimes.

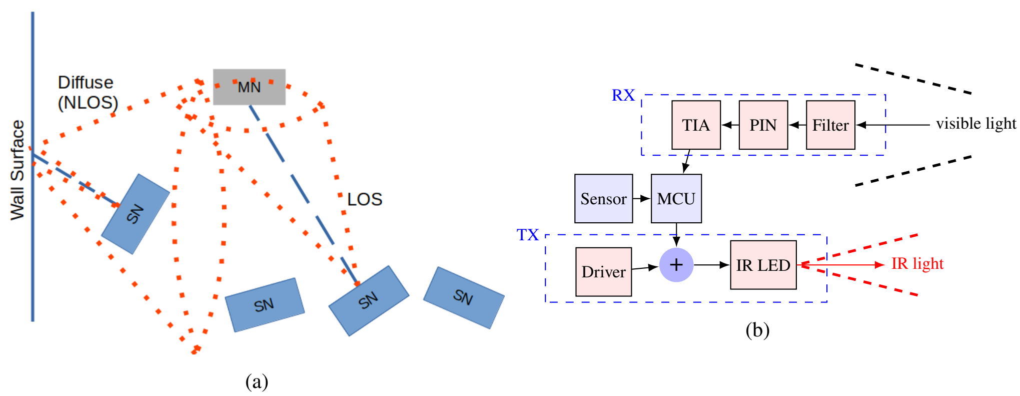

Fig. 1. (a) Hybrid VLC/IR network architecture and (b) SN subsystem.

The contribution of the present work lies in several areas. First of all, we provide a more practical analysis of the OWC-based WSN. Compared to our previous work [24], where we only considered LOS, in this work, we now account for the contribution of diffuse light resulting from beam reflections at various room surfaces. For relatively high data-rate links, it is well known that such reflections may result in inter-symbol interference (ISI) [25]. However, we initially use a ray tracing scheme to show that the optical wireless channel can be considered approximately flat for the data rates considered in typical IoT applications (i.e., of the order of kb/s). Therefore, at the MN RX, diffuse radiation simply adds up to the LOS contribution, thus improving the signal-to-noise ratio (SNR). This implies prolonged battery life, which is highly desirable in WSNs.

Second, we provide an efficient and low-complexity received power estimation scheme in order to estimate the link budget, taking into account the diffuse light contribution. Our approach is, in fact, a simplified version of the impulse response estimation model presented in [26]. Since the diffuse channel can be considered as flat, there is no need to track arrival times of the diffuse components, and hence the power estimation is considerably simplified requiring much less computational time and memory resources, compared to full-blown ray tracing simulations.

Third, we adopt a machine-learning approach based on a specially tailored genetic algorithm (GA) [27] to optimize link design in terms of the battery life time. Using established diffuse impulse response estimation models such as those based on ray-tracing would render such optimizations impractical. Our simplified link budget model discussed above, however, renders such optimizations feasible. Various parameters are included in the optimization pertinent to the SN/MN arrangement considering the indoor environment (wall configuration, surface reflectivity, etc). To the best of the authors knowledge, such an application of a GA for optimizing the optical wireless link parameters in the context of IoT applications has not been reported in the literature.

The fourth area of our contribution is the fact that, as evidenced by the obtained results, the achieved battery life times of the SNs are considerable, indicating the potential of optical wireless for WSNs. We pay special attention to scenarios where no LOS power is received (e.g. due to blocking) and show that optimizing the TX beam-width can lead to significant power savings. Our results can therefore pave the way for adopting optical wireless technologies in the context of WSNs and IoT.

It is worth mentioning that, in every system optimization problem, there are two basic ingredients: the system model and the optimization engine. The rest of the paper is organized in order to reflect these two points. Section 2 describes the model developed to describe the OWC link and the energy usage for the application scenario at hand. Initially, we use ray-tracing to show that in typical indoor scenarios, the diffuse channel is effectively flat and can therefore be simply described by a channel gain coefficient. We then outline how the received diffuse power can be efficiently calculated. For a target up-link bit error rate (BER), we can therefore estimate the required transmission power and the driving current at the LED of the SN. Given the transmission cycle of the SN, this information can also be used to estimate the battery life time. The model of Section 2 then feeds a GA to optimize the battery life of the SNs, which is outlined in Section 3. Next, Section 4 presents the results obtained and their impact on WSN-based applications. Section 5 concludes the paper, providing also a research outlook.

2. System Model

We consider two rooms of different dimensions as outlined in Table 1. Configuration A is a small room and is identical to the one considered in [26], whereas configuration B is a larger room indicative of office spaces, storage rooms, etc. The reflectivity values in Table 1 correspond to typical white paint on plasterboard or acoustic tiles for the sidewalls/ceiling and light gray tiles for the floor.

2.1. Optical wireless channel

The OWC channel is a linear, time invariant (LTI) system described by its impulse response $h(t)$. The LOS contribution is described by a Dirac delta function $h_{\mathrm{MN}}\delta(t - t_{\mathrm{MN}})$ [26], where h_{MN} is the LOS channel gain, $t_{\mathrm{MN}} = R_{\mathrm{MN}}/c$ the propagation delay between the SN and the MN, R_{MN} their distance and c the speed of light. The total impulse response $h(t)$ equals the sum of the LOS and the diffuse light component $h_{\mathrm{D}}(t)$, i.e.:

$$h(t) = h_{\mathrm{MN}}\delta(t - t_{\mathrm{MN}}) + h_{\mathrm{D}}(t) \tag{1}$$

We use an in-house `Python` implementation of the modified Monte Carlo ray-tracing method [28] to obtain $h_{\mathrm{D}}(t)$ and then use the fast Fourier transform (FFT) to determine the diffuse channel frequency response $H_{\mathrm{D}}(f) = \mathscr{F}\{h_{\mathrm{D}}(t)\}$, where $\mathscr{F}\{\cdot\}$ denotes the Fourier transform. We assume purely diffusive ideal Lambertian reflectors.

Figure 2 shows $H_{\mathrm{D}}(f)$ obtained for the up-link for configurations A and B of Table 1 and for MN positioned in the middle of the ceiling, $\mathbf{r}_{\mathrm{MN}} = [L/2, W/2, H]$ while the SN is

Table 1. Simulation parameters

Parameter	Config. A	Config. B
Length, L	5 m	10 m
Width, W	5 m	10 m
Height, H	3 m	4 m
Window height, H_w	1 m	2 m
Window width, W_w	1 m	2 m
Peak spectral irradiance, p_n	2 W/nm/m^2	
Ambient light temperature, T_K	5800 K	
Wall reflectivity, ρ_w	0.8	
Ceiling reflectivity, ρ_c	0.8	
Floor reflectivity, ρ_f	0.3	
MN field-of-view, FOV_{MN}	$\pi/2$	
SN field-of-view, FOV_{SN}	$\pi/2$	
MN orientation, $\mathbf{n}_{MN}$	$\hat{\mathbf{z}}$	
SN orientation, $\mathbf{n}_{SN}$	$-\hat{\mathbf{z}}$	
MN transmission power, P_{MN}	6 W	
Maximum SN transmission power, P_{SN}	25 mW	
IR LED half intensity angle, $\Phi_{1/2}$	60°	
IR LED pattern order, m	1	
IR LED driver curve	TSFF5210 [24]	
Max SN driver current, I_{max}	100 mA	
Responsivity model	BPV10NF [24]	
VLC rejection filter model	VTB5051BH [24]	
IR rejection filter model	BPV10NF [24]	
Maximum data rate, R_{max}	10 kb/s	
Target error rate, BER_0	10^{-3}	
Spectral efficiency, η_{eff}	0.4 bit/s/Hz	
Up-link message length, L_u	200 bits	
Down-link message length, L_d	200 bits	
Feedback resistance, R_F	1 MΩ	
Modulation type	OOK	
RMS voltage noise density, V_{rms}	15 nV/$\sqrt{\text{Hz}}$	
RMS current noise density, V_{rms}	400 fA/$\sqrt{\text{Hz}}$	
Voltage noise corner frequency, f_{cv}	1 kHz	
Current noise corner frequency, f_{ci}	1 kHz	
Sleep mode current, I_{SL}	400 nA	
Wake-up current, I_{WU}	1.3 mA	
Read out current, I_{RO}	1.3 mA	
Wake-up time, t_{WU}	20 ms	
Read-out time, t_{RO}	40 ms	
Cycle period, t_{CY}	1 min	
Battery capacity, Q_{TOT}	220 mAh	

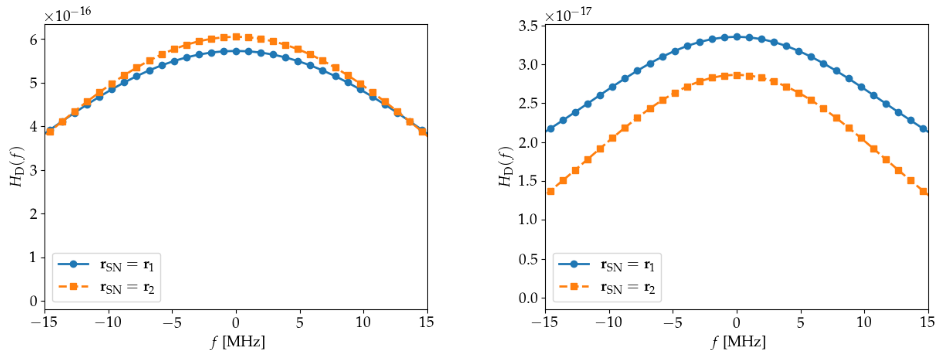

(a) (b)

Fig. 2. Diffuse channel impulse response $|H_{\mathrm{D}}(f)|$ for: a) configuration A and b) configuration B.

positioned at two different locations along the floor diagonal: $\mathbf{r}_{\mathrm{SN}} = \mathbf{r}_1 = [L/2, W/2, 0]$ and $\mathbf{r}_{\mathrm{SN}} = \mathbf{r}_2 = [L/4, W/4, 0]$. The SN and MN are directed according to Table 1. Figure 2a, corresponding to configuration A, shows that for both SN positions, $H_{\mathrm{D}}(f)$ varies in the MHz-range and can therefore be considered effectively flat in the sub-MHz frequency range. The half width 1 dB bandwidth $B_{1\mathrm{dB}}$ values of $|H_{\mathrm{D}}(f)|^2$ are 8.2 and 7.3 MHz for $\mathbf{r}_{\mathrm{SN}} = \mathbf{r}_1$ and $\mathbf{r}_{\mathrm{SN}} = \mathbf{r}_2$ respectively. A similar behavior is obtained for configuration B, where $B_{1\mathrm{dB}}$ is now 7.2 and 5.3 MHz for $\mathbf{r}_{\mathrm{SN}} = \mathbf{r}_1$ and $\mathbf{r}_{\mathrm{SN}} = \mathbf{r}_2$, respectively. These results indicate that the diffuse channel can be considered flat for WSN applications and can therefore be described by a scalar channel gain coefficient h'_{MN}. The total channel gain will simply be equal to the sum of the LOS and diffuse channel gains:

$$h_{\mathrm{MN}}^{\mathrm{TOT}} = h_{\mathrm{MN}} + h'_{\mathrm{MN}} \tag{2}$$

where

$$h'_{\mathrm{MN}} = \int_{-\infty}^{+\infty} h_{\mathrm{D}}(t)\mathrm{d}t \tag{3}$$

There are two basic aspects of the physical layer model that we present in this section: the link budget model discussed in subsection 2.2 and the transceiver model discussed in subsection 2.3 which includes power consumption.

2.2. Diffuse power and link budget

Assuming a generalized Lambertian-type TX of order m, located at $\mathbf{r} = \mathbf{r}_{\mathrm{S}}$, oriented along the unitary vector $\mathbf{n}_{\mathrm{S}}$, and a receiver placed at $\mathbf{r} = \mathbf{r}_{\mathrm{R}}$, which is oriented along $\mathbf{n}_{\mathrm{R}}$ and has an effective area A_{R} and field-of-view equal to FOV, the channel gain is determined by:

$$h(\mathbf{r}_{\mathrm{R}}, \mathbf{n}_{\mathrm{R}}, \mathbf{r}_{\mathrm{S}}, \mathbf{n}_{\mathrm{S}}) = \frac{m+1}{2\pi R^2} \cos^m \phi \cos\theta A_{\mathrm{R}} U \left(\frac{\theta}{\mathrm{FOV}}\right) \tag{4}$$

where

$$\cos\theta = \frac{\mathbf{n}_{\mathrm{R}} \cdot (\mathbf{r}_{\mathrm{S}} - \mathbf{r}_{\mathrm{R}})}{R} \tag{5a}$$

$$\cos\phi = \frac{\mathbf{n}_{\mathrm{S}} \cdot (\mathbf{r}_{\mathrm{R}} - \mathbf{r}_{\mathrm{S}})}{R} \tag{5b}$$

$$R = |\mathbf{r}_{\mathrm{S}} - \mathbf{r}_{\mathrm{R}}| \tag{5c}$$

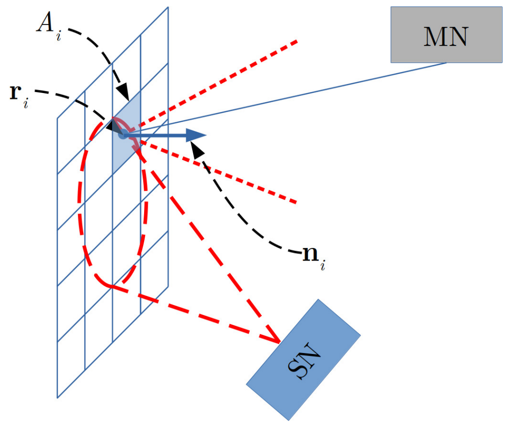

Fig. 3. Estimation of the diffuse light channel gain.

As part of our optimizations and in order to avoid adopting time-consuming ray-tracing schemes as in Section 2.1, we use a faster simulation method, where all room surfaces are represented by a collection of elementary sub-surfaces A_i, as shown in Figure 3. We first calculate the incident power $P_i^{(1)}$ on each A_i from the SN using (4), i.e., at the first light bounce. We also calculate the intra-subsurface LOS gain h_{qp} assuming A_p and A_q are the TX and the RX, respectively. For A_p, the transmit power is $r_p P_p^{(0)}$, where r_p is the reflectivity of A_p. Following the second bounce, the power received by A_q is written as the sum of powers received by all other elementary surfaces. More generally, the power received at the b^{th} bounce is given by:

$$P_q^{(b)} = \sum_{p=1}^{N_{\text{E}}} h_{qp} r_p P_p^{(b-1)} \tag{6}$$

In (6), N_{E} is the number of elementary surfaces within the room. If h_q^{MN} are the channel gains assuming A_q is the TX and MN the RX, then the diffuse-light power $P_{\text{D}}^{(b)}$ is the sum of the received power from all A_q and therefore, the total diffuse power is given as:

$$P_{\text{D}} = \sum_{b=1}^{N_{\text{B}}} P_{\text{D}}^{(b)} = \sum_{b=1}^{N_{\text{B}}} \sum_{q=1}^{N_{\text{E}}} h_q^{\text{MN}} r_q P_q^{(b)} \tag{7}$$

where h_q^{MN} is the channel gain between A_q and the MN. Using (6) and (7) is analogous to the impulse response estimation adopted in [26], except that the channel here is considered to have flat response, and hence we simply add power contributions from consecutive bounces, speeding up computations significantly.

Assuming the SN is positioned on various points along the diagonal $\mathbf{r}_{\text{SN}} = [x, x, 0]$ and its orientation is vertical, i.e. $\mathbf{n}_{\text{SN}} = \hat{\mathbf{z}}$, we have investigated the power distribution profiles $P_{\text{D}}^{(b)}$ in Figure 4a for configuration B. Interestingly enough, the power for $b = 1$ is smaller than $b = 2$. For $b = 1$, most of the IR power illuminates the ceiling elements and therefore lies outside the field-of-view (FOV) of the MN. For $b = 2$, the MN captures optical power from sidewall elements that are now illuminated by the ceiling. Figure 4b, depicts the power distribution profiles for the LOS and diffuse paths, as well as the total power level for configuration B. Note that, near the center of the diagonal ($x \cong L/2$), the LOS path is much stronger than the diffuse path. This is because for $x \cong L/2$, the alignment is optimal, since both $\mathbf{r}_{\text{SN}}$ and $\mathbf{r}_{\text{MN}}$ lie on the line between the transceivers. Near the edges of the room, the diffuse component contributes greatly to the total received power, since alignment is worse.

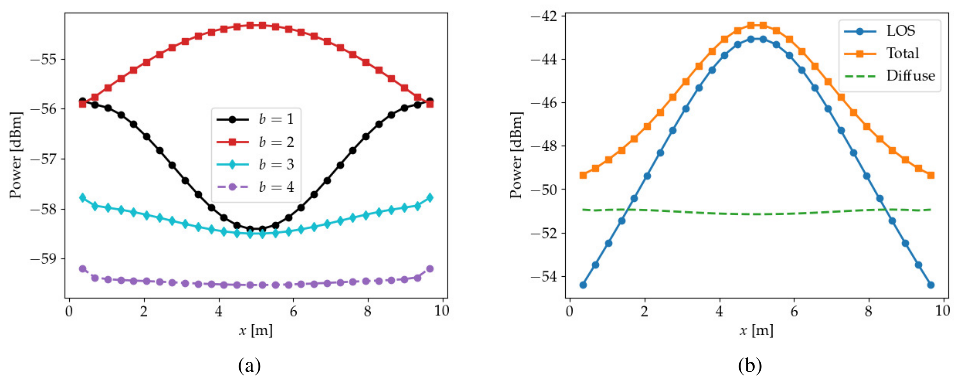

Fig. 4. a) Diffuse power contribution depending on bounce b and b) comparison of each propagation path contribution to the received power.

2.3. Transceiver model and energy efficiency

The transceiver model includes the transmission spectra of nodes, RX filter spectra, photodiode responsivity, ambient light noise and TIA noise. Here we briefly describe the model features and the interested reader is referred to [24] for an in-depth analysis.

The SN transceiver is modeled based on the characteristics of the TSFF5210 IR LED and the VTB5051BH silicon photodiode with an IR rejection filter (Table 1). The IR LED transmission spectra $S_{\mathrm{T}}(\lambda)$ is described by a Gaussian profile with a full width at half maximum (FWHM) of $\Delta\lambda = 40$ nm, peaking around $\lambda = 870$ nm. The optical power-current characteristic $P_{\mathrm{T}} = f(I_{\mathrm{D}})$ is obtained by polynomial fitting of the actual light-current curve of TSFF5210. We assume a super-Gaussian profile for the IR rejection filter of order 3 with a 10 dB bandwidth of 230 nm peaking at 435 nm while the responsivity $\mathcal{R}(\lambda)$ of the detector is described by a polynomial with respect to λ with coefficients extrapolated by curve-fitting from the BPV10NF responsivity.

The MN transceiver is modeled based on typical spectra of warm white phosphorescent LEDs [29]. We describe the transmission spectra using a sum of two Gaussian profiles, corresponding to the blue and the phosphor components peaking at 470 and 600 nm, respectively, with FWHM equal to 20 and 100 nm, respectively. The daylight blocking filter is described by a 3rd order super-Gaussian peaking at 870 nm with a 10 dB bandwidth of 300 nm. Given the spectral properties of the transceiver, we determine the effective responsivity $\mathcal{R}_{\mathrm{eff}}$ describing the matching between the transmission spectra, the receiver's rejection filter and responsivity. Following the approach of [24], we obtain 0.49 and 0.32A/W for $\mathcal{R}_{\mathrm{eff}}$ in the up-link and down-link, respectively.

The RX noise is mainly due to the ambient light-induced shot noise and the TIA thermal noise, where the former is usually dominant and can be characterized by its spectral irradiance, which in our model follows a black-body radiation model with an absolute temperature of 5800 K. Given the position and orientation of the emitting surfaces (e.g. windows), (4) can be modified to estimate the ambient light power incident at the RX. We assume a 1 and 4 m^2 window for configurations A and B, respectively, (Table 1) with a peak spectral irradiance of 2 W/nm/m^2. We note that, $\mathcal{R}_{\mathrm{eff}}$ for ambient light is 0.09 A/W for the MN and 0.13 A/W for the SN [24]. Assuming on/off keying (OOK) modulation, then for a given SNR the transmit power P_{T} and thus the LED drive current I_{D} can be determined. The energy usage at the SN can be calculated considering the currents drawn by the transceiver and the MCU during various phases. Table 1 quotes typical values for each cycle [24]. Based on these, we can calculate the charge Q_{CY} drawn from the battery at each cycle and determine the node battery lifetime t_{BL} given the battery capacity Q_{TOT} (assumed 220 mAh, typical of a coin-cell battery).

3. Link Optimization

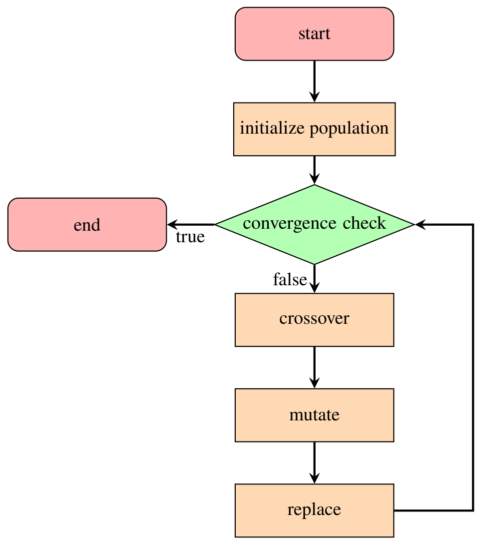

Fig. 5. The flowchart of the genetic algorithm used in this work.

In Figure 5, we show the flowchart of the GA used to optimize the system parameters such as the SN orientation and data rate. Initially, we randomly choose a population consisting of N_{INIT} realizations of the system (chromosomes). The algorithm then proceeds to select candidates by generating offsprings using a *crossover* operation, which transfers part of the parent genes to the offsprings. The genes of the offsprings are also *mutated*, i.e. randomly changed in an attempt to increase diversity. If a chromosome is produced that is stronger than the weakest chromosome in the existing pool, then the former chromosome is replaced by the latter. We then carry out a convergence check to see whether the algorithm's termination criteria are met and if not, we repeat the previous steps.

In each iteration, the strongest 50 % of the chromosomes constitute the mating pool. We choose two parents through tournament selection and we calculate the offspring using uniform crossover, which consists of tossing an unbiased coin and randomly selecting the value of each offspring gene from either the first or the second parent. The mutation is achieved by adding a random correction factor Δv_k to each of the offspring genes v_k. The corrections are determined by $\Delta v_k = \alpha \beta_k v_k$, where $0 \leq \alpha \leq 1$ is the *mutation factor*, and β_k are randomly chosen from a uniform distribution inside $[-1, 1]$. The chromosome values considered for the optimization are the inclination and azimuth angles θ and ϕ, respectively, as well as the data rate R_{b}. The angles determine the orientation of the SN, $\mathbf{n}_{\text{SN}} = [\cos\phi \sin\theta, \sin\phi \sin\theta, \cos\theta]$, while R_{b} is related to the required bandwidth B and the transmission time t_{TX}. Note that, the strength of each chromosome is determined by a fitness function. In our case, we let t_{BL} determine the fitness of each system in order to optimize the energy efficiency at the SN. It is important to ensure that the maximum driving current should not exceed a specified value $I_{\max}$ due to the LED specifications, see Table 1. If this condition is not met, we set the fitness value equal to zero to avoid a non-viable solution.

The overall model including the GA which is available under an open-source license [30], is implemented in `Python` using standard libraries such as `numpy`, `scipy` and `matplotlib`. In order to speed-up the code execution, we choose to rely on vectorization, avoiding loops as much as possible. For example, it is much more efficient to determine all intra-channel gains h_{qp} simultaneously using a vector/matrix approach. In addition we only need to calculate h_{qp} once, since they only depend on the positioning and orientation of the sub-surfaces A_q. This speeds up the fitness evaluations considerably. In our simulations we also took advantage of `Python`'s `multiprocessing` package to distribute computations in multiple processor cores. The full link and energy consumption models and the optimization engine of our proposed approach, implemented in `Python`, are freely made available under an open-source license [30].

4. Results and Discussions

In the proposed optimization scheme, we seek to determine the optimal values of $[\phi, \theta, R_{\mathrm{b}}]$ for every position in the floor diagonal $\mathbf{r}_{\mathrm{SN}} = [x, x, 0]$. We examine three cases: in the first and second variations, we only account for either the LOS or diffuse light power, respectively, when calculating t_{BL}. In the third variation, we sum up both contributions. The population has $N_{\mathrm{INIT}} = 50$ chromosomes and we use a mutation factor $\alpha = 0.1$. The algorithm terminates when either a maximum number of crossovers occurs (in our case 20000) or the population's fitness values f_i do not differ significantly from each other. The population fitness smoothness is determined as $S = (f_{\max} - f_{\min})/f_{\max}$ where $f_{\max}$ and $f_{\min}$ are the maximum and minimum values of f_i, respectively. We terminate the algorithm if $S < 0.05\%$.

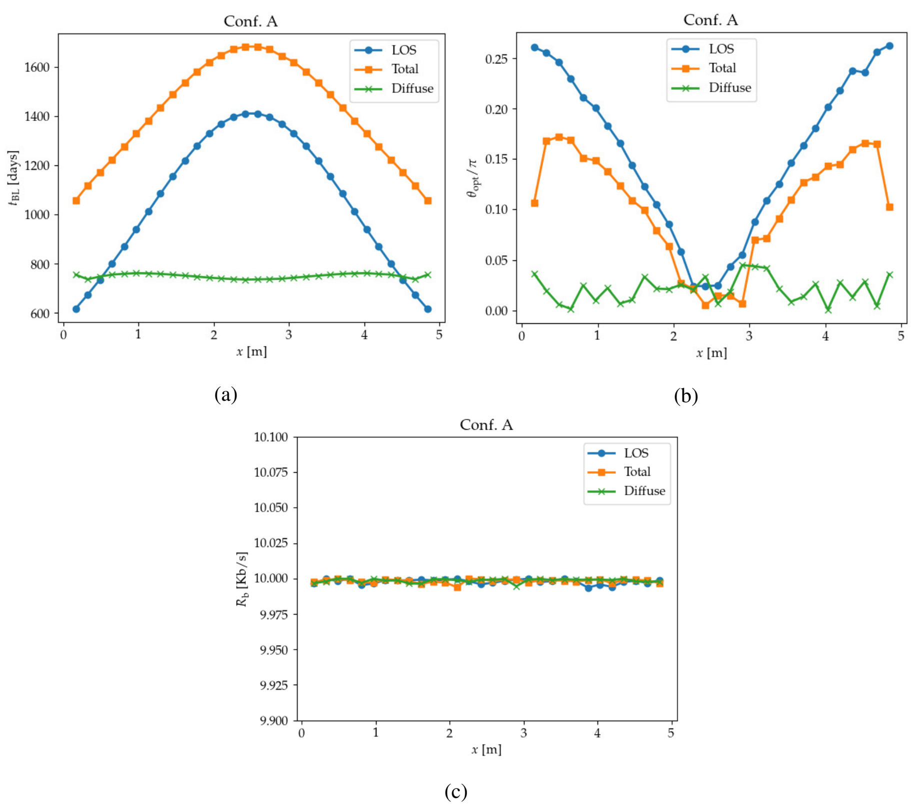

Fig. 6. Optimization results for room configuration A: a) battery lifetime, b) optimal elevation angle and c) optimal data rate

Figure 6a depicts the fitness function (i.e. t_{BL}) across the diagonal of the room $[x, x, 0]$ obtained by the GA for configuration A, assuming LOS, diffuse and a combination of both. It is

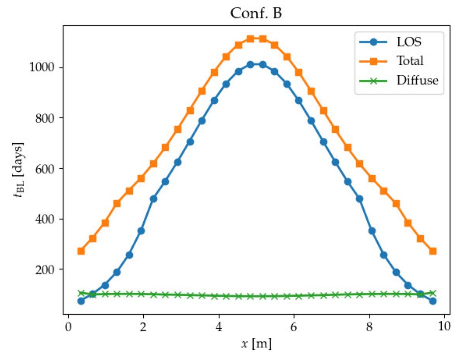

(a)

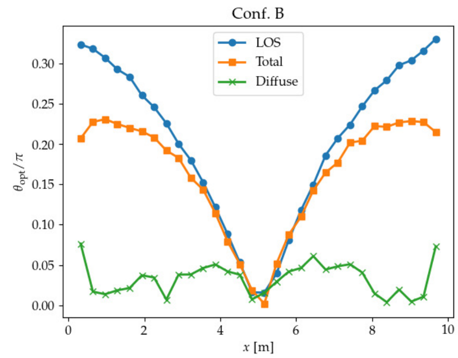

(b)

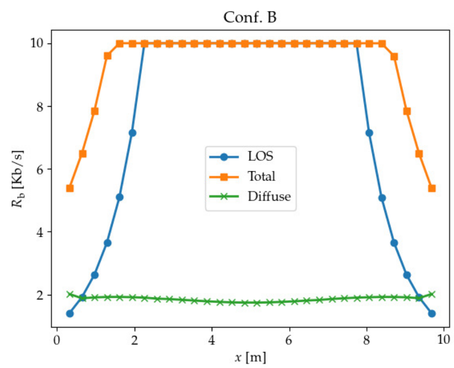

(c)

Fig. 7. Optimization results for room configuration B: a) battery lifetime, b) optimal elevation angle and c) optimal data rate

interesting to note that the LOS component t_{BL} is symmetrical around 2.5 m with a peak value of 1400 days dropping at a rate of 400 day/m compared to the diffuse, which is almost flat at 750 days, for $0 \leq x \leq 5$ m. This is due to the fact that as the MN/SN distance is increased, the power budget worsens. Considering both LOS and diffuse components, energy efficiency is improved particularly near the edges of the diagonal. Figures 6b and 6c show the optimal elevation angle θ and the data rate R_{b}. For LOS, the optimal θ increases when we move away from the center ($x = 2.5$ cm) to better align with the MN, whereas the diffuse scenario favors $\theta \approx 0$, in which case the SN is almost pointing directly upwards, $\mathbf{n}_{\mathrm{SN}} \approx \hat{\mathbf{z}}$. The obtained data rate is given by $R_{\mathrm{b}} \approx 10$ kb/s $= R_{\max}$, which is the maximum allowable value given by system constraints. The fact that higher R_{b} are favored can be explained through the RX electrical SNR in the case of OOK, given as:

$$\mathrm{SNR} = \frac{R_{\mathrm{eff}}^2 P_{\mathrm{R}}^2}{2\sigma^2} \tag{8}$$

where P_{R} is the received optical signal power (proportional to the transmit power P_{T}) and σ^2 is the RX noise power. Neglecting the TIA noise, we have $\sigma^2 = 2qI_{\mathrm{amb}}B$, where I_{amb} is the DC current due to ambient light, q is the electron charge, $B = R_{\mathrm{b}}/\eta_{\mathrm{eff}}$, the signal bandwidth and η_{eff} is the spectral efficiency. Thus, with reference to (8), $P_{\mathrm{T}} \propto \sqrt{R_{\mathrm{b}}}$. Assuming linear light-current characteristic at the SN LED, we can also deduce that $I_{\mathrm{D}} \propto \sqrt{R_{\mathrm{b}}}$. Since the duration of the transmission phase t_{TX} is proportional to the bit duration $1/R_{\mathrm{b}}$, we readily see that the charge drawn from the node battery is $Q_{\mathrm{TX}} \propto 1/\sqrt{R_{\mathrm{b}}}$. This implies that provided that $I_{\mathrm{D}} \leq I_{\max}$,

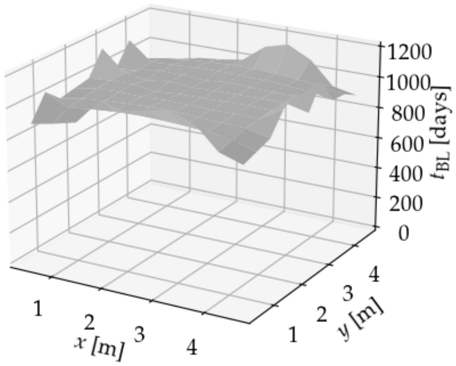

(a)

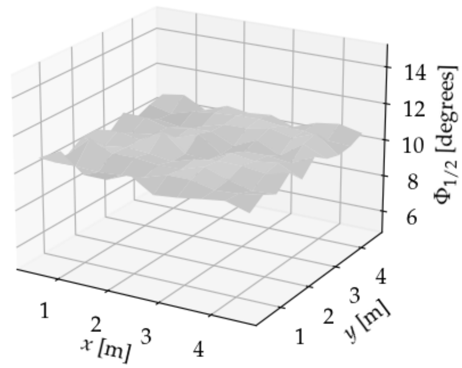

(b)

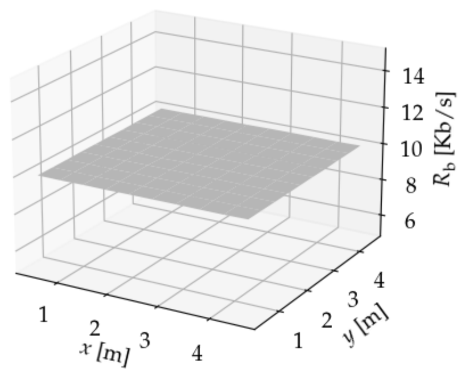

(c)

Fig. 8. Optimization results for diffuse light propagation configuration A: a) t_{BL}, b) $\Phi_{1/2}$ and c) R_{b}.

increasing R_{b} leads to improved energy efficiency.

Figure 7 shows the optimized results for configuration B. As shown in Figure 7a, the diffuse path offers the lowest battery lifetime with an average of $\approx$ 96 days. However it can still increase the overall battery lifetime considerably, especially at the edges of the diagonal. The optimal elevation angles exhibit a similar variation as those in Figure 6b, implying that if the diffuse component alone is considered, the optimal SN orientation is still $\mathbf{n}_{\mathrm{SN}} \approx \hat{\mathbf{z}}$. As expected, the optimal SN elevation angles increase with the distance from the floor center, in order to improve SN/MN alignment. Figure 7c depicts the optimal data rate, which is not always $\approx$ 10 kb/s since the required driving current must not exceed I_{max}. Considering only the diffuse component, the optimal $R_{\mathrm{b}} \approx 2$ kb/s. For the LOS component, R_{b} is much higher except for the points near the edge of the diagonal. Assuming both contributions from LOS and diffuse paths, we obtain an optimal data rate $\geq$5 kb/s for all SN positions considered (orange curve in Figure 7c).

For the LOS path, an obvious way to improve the link budget is to choose a smaller beam-width $\Phi_{1/2}$ thereby reducing beam spreading at the expense of tighter alignment control and limited mobility. It is interesting to investigate the optimal beam pattern for the diffuse path as well

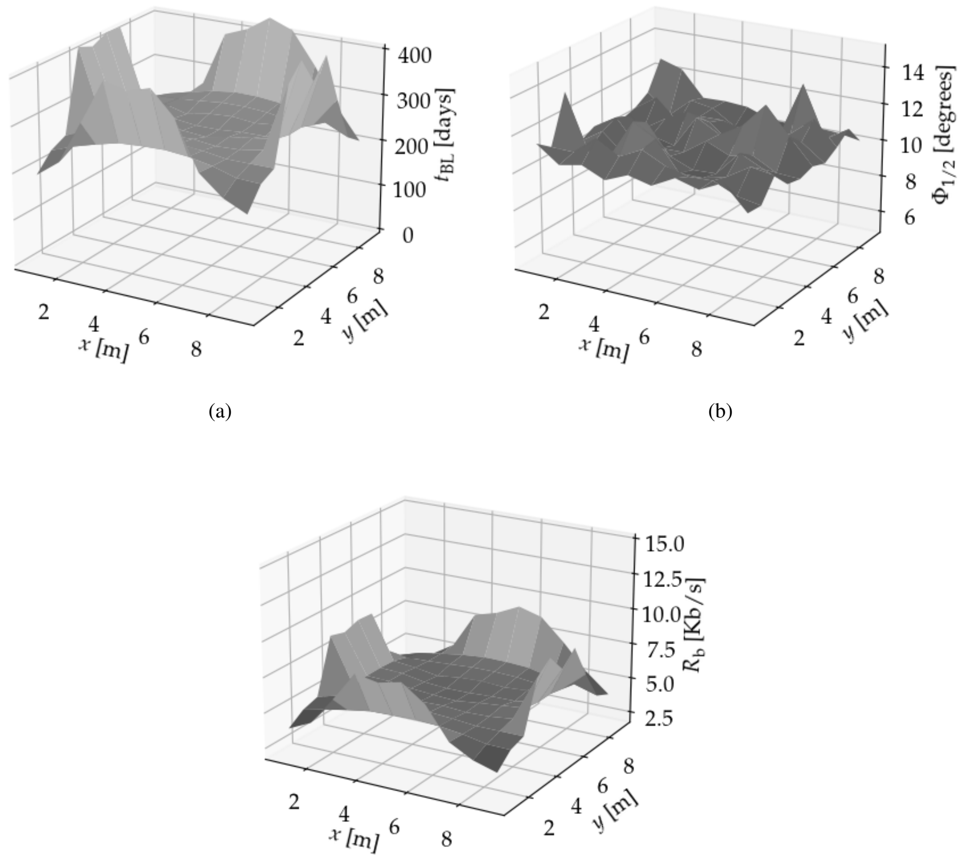

(a)

(b)

Fig. 9. Optimization results for diffuse light propagation configuration B: a) t_{BL}, b) $\Phi_{1/2}$ and c) R_{b}.

considering many possible positions for the SN. Figures 8 and 9, show the results for the two room configurations assuming that the beam-width $\Phi_{1/2}$ is also included in the optimization inside a range of $[10°, 20°]$. Figures 8a, 8b, and 8c depict the values of t_{BL}, $\Phi_{1/2}$ and R_{b} respectively obtained for configuration A, assuming a 10×10 grid on the floor of the room. A minimum value of t_{BL} obtained was 890 days at the room corners. The optimal value for $\Phi_{1/2}$ was near $10°$. This does not change even if we widen the allowed range for $\Phi_{1/2}$ in the GA and indicates a non-directed scenario where a tight beam impinges on the nearby room sidewall and light reaches the MN by a diffuse path. For all SN positions considered, the optimal R_{b} obtained is $\cong$ 10 kb/s. The results for configuration B are shown in Figure 9. In this case, the minimum value of t_{BL} is 186 days and is maximized near the sidewalls reaching up to 450 days. Again, the algorithm favors beam-widths near $10°$ while the optimal data rate ranges from 3.6 to 9.4 kb/s.

5. Conclusions and future directions

In this work, we took a deeper look at the potential of optical technologies for WSNs and IoT applications, which are relevant for mMTC applications within 5G and beyond networks. We presented a realistic model for describing a hybrid VLC/IR WSN, which included diffuse-light propagation. We showed that for typical data rates pertinent to most indoor mMTC applications, the diffuse channel can be effectively considered flat and simply be described by a channel gain. This allowed us to implement an efficient link budget model that can be used to significantly speed up computations in system optimizations. To maximize battery life, we used a machine learning approach based on a GA to optimize MN/SN configurations and showed that substantially increased SN battery lifetimes are obtained, even for coin-cell battery capacities. We also investigated scenarios where only the diffuse light contribution was considered and the SN TX beam-widths were included in the optimization. For data rates envisioned in such applications, diffuse light propagation can improve the up-link power budget as well as energy efficiency. This is true for both small and larger room configurations such as those examined in this work. The optimizations show that when the LOS path is blocked, the diffuse path actually favors non-directed configurations with narrower beam-widths, where the IR light is aimed at the room's sidewalls, reaching the MN via single and multiple bounces. Both the proposed model and the optimization engine are available freely on the web under an open-source license for other researchers to use and can form a basis, where GA optimizations can be carried out possibly applying different channel modeling approaches for indoor [31] or even underwater systems [32].

The results obtained in this paper point towards some interesting research directions to implement VLC/IR WSNs. A key question is whether the SN configuration can be changed in an adaptive manner. One could envision controlling the IR LED radiation pattern using micro-electromechanical systems [33] while the direction of transmission could be also controlled using low-cost servo-motors mounted at the SN. It would also be interesting to develop algorithms for the real-time optimization of the up-link performance that can converge quickly, to limit power dissipation during the optimization stage. Another interesting scenario would be to investigate multi-hop scenarios where SNs, which are far from the MN or their LOS paths might experience shadowing and blocking, communicate with the MN via other SNs. It is our intention to investigate some of these research directions as part of our future research.

Funding. This publication was based upon work from COST (European Cooperation in Science and Technology) Action NEWFOCUS CA19111.

References

1. S. Nižetić, P. Šolić, D. L.-d.-I. González-de, L. Patrono *et al.*, "Internet of things (iot): Opportunities, issues and challenges towards a smart and sustainable future," J. Clean. Prod. **274**, 122877 (2020).
2. H. C. Leligou, T. Zahariadis, L. Sarakis, E. Tsampasis, A. Voulkidis, and T. E. Velivassaki, "Smart grid: a demanding use case for 5g technologies," in *2018 IEEE International Conference on Pervasive Computing and Communications Workshops (PerCom Workshops),* (IEEE, 2018), pp. 215–220.
3. R. Giuliano, F. Mazzenga, and A. Vizzarri, "Satellite-based capillary 5g-mmtc networks for environmental applications," IEEE Aerosp. Electron. Syst. Mag. **34**, 40–48 (2019).
4. F. Franchi, F. Graziosi, A. Marotta, and C. Rinaldi, "Structural health monitoring over 5g urllc network," in *European Workshop on Structural Health Monitoring,* (Springer, 2020), pp. 60–68.
5. S. Horsmanheimo, J. Säe, T. Jokela, L. Tuomimäki, E. Nigussie, A. Hjelt, S. Huilla, T. Dönmez, N. Le Bail, and M. Valkama, "Remote monitoring of iot sensors and communication link quality in multisite mmtc testbed," in *2019 IEEE 30th Annual International Symposium on Personal, Indoor and Mobile Radio Communications (PIMRC),* (IEEE, 2019), pp. 1–7.
6. B. Wang, Y. Sun, C. Yuan, and X. Xu, "Lesla: A smart solution for sdn-enabled mmtc e-health monitoring system," in *Proceedings of the 8th ACM MobiHoc 2018 Workshop on Pervasive Wireless Healthcare Workshop,* (2018), pp. 1–6.
7. W. Saad, M. Bennis, and M. Chen, "A vision of 6g wireless systems: Applications, trends, technologies, and open research problems," IEEE network **34**, 134–142 (2019).
8. X. Li, D. Li, J. Wan, A. V. Vasilakos, C.-F. Lai, and S. Wang, "A review of industrial wireless networks in the context of industry 4.0," Wirel. networks **23**, 23–41 (2017).
9. H. Aslanyan and J. Rolim, "Interference minimization in wireless networks," in *2010 IEEE/IFIP International Conference on Embedded and Ubiquitous Computing,* (IEEE, 2010), pp. 444–449.
10. J. M. Kahn and J. R. Barry, "Wireless infrared communications," Proc. IEEE **85**, 265–298 (1997).
11. H. Haas, L. Yin, Y. Wang, and C. Chen, "What is lifi?" J. lightwave technology **34**, 1533–1544 (2016).

12. L. Bariah, L. Mohjazi, S. Muhaidat, P. C. Sofotasios, G. K. Kurt, H. Yanikomeroglu, and O. A. Dobre, "A prospective look: Key enabling technologies, applications and open research topics in 6g networks," IEEE access **8**, 174792–174820 (2020).
13. M. Müller, D. Behnke, P.-B. Bök, C. Kottke, K. L. Bober, and V. Jungnickel, "Leverage lifi in smart manufacturing," in *2020 IEEE Globecom Workshops (GC Wkshps,* (IEEE, 2020), pp. 1–6.
14. V. Jungnickel, M. Hinrichs, K. Bober, C. Kottke, A. Corici, M. Emmelmann, J. Rufo, P.-B. Bök, D. Behnke, M. Riege *et al.*, "Enhance lighting for the internet of things," in *2019 Global LIFI Congress (GLC),* (IEEE, 2019), pp. 1–6.
15. G. Schirripa Spagnolo, L. Cozzella, and F. Leccese, "Underwater optical wireless communications: Overview," Sensors **20**, 2261 (2020).
16. X. Chen, J. Ding, B. Yu, H. Ma, and H. Lai, "A survey on wireless optical its for smart city," in *Asia Communications and Photonics Conference,* (Optical Society of America, 2019), pp. M4A–110.
17. Y. Mekonnen, S. Namuduri, L. Burton, A. Sarwat, and S. Bhansali, "Machine learning techniques in wireless sensor network based precision agriculture," J. Electrochem. Soc. **167**, 037522 (2019).
18. S. Riurean, T. Antipova, Á. Rocha, M. Leba, and A. Ionica, "Vlc, occ, ir and lifi reliable optical wireless technologies to be embedded in medical facilities and medical devices," J. medical systems **43**, 1–10 (2019).
19. M. F. Ahmed, M. K. Hasan, M. Z. Chowdhury, N. C. Hoan, and Y. M. Jang, "Continuous status monitoring of industrial valve using occ-enabled wireless sensor network," IEEE Transactions on Instrumentation Meas. (2021).
20. B. Donmez, R. Mitra, and F. Miramirkhani, "Channel modeling and characterization for vlc-based medical body sensor networks: Trends and challenges1," IEEE Access (2021).
21. O. Haddad, M.-A. Khalighi, S. Zvanovec, and M. Adel, "Channel characterization and modeling for optical wireless body-area networks," IEEE Open J. Commun. Soc. **1**, 760–776 (2020).
22. P. Agheli, H. Beyranvand, and M. J. Emadi, "Uav-assisted underwater sensor networks using rf and optical wireless links," J. Light. Technol. **39**, 7070–7082 (2021).
23. X. Liu, X. Wei, L. Guo, Y. Liu, Q. Song, and A. Jamalipour, "Turning the signal interference into benefits: Towards indoor self-powered visible light communication for iot devices in industrial radio-hostile environments," IEEE Access **7**, 24978–24989 (2019).
24. T. Kamalakis, Z. Ghassemlooy, S. Zvanovec, and L. N. Alves, "Analysis and simulation of a hybrid visible-light/infrared optical wireless network for iot applications," J. Opt. Commun. Netw. **14**, 69–78 (2022).
25. G. Ntogari, T. Kamalakis, and T. Sphicopoulos, "Performance analysis of non-directed equalized indoor optical wireless systems," in *2008 6th International Symposium on Communication Systems, Networks and Digital Signal Processing,* (IEEE, 2008), pp. 156–160.
26. J. R. Barry, J. M. Kahn, W. J. Krause, E. A. Lee, and D. G. Messerschmitt, "Simulation of multipath impulse response for indoor wireless optical channels," IEEE journal on selected areas communications **11**, 367–379 (1993).
27. T. Kamalakis, L. Dogkas, and F. Simou, "Optimization of a discrete multi-tone visible light communication system using a mixed-integer genetic algorithm," Opt. Commun. **485**, 126741 (2021).
28. J. Lopez-Hernandez, R. Perez-Jimenez, and A. Santamaria, "Modified monte carlo scheme for high-efficiency simulation of the impulse response on diffuse ir wireless indoor channels," Electron. Lett. **34**, 1819–1820 (1998).
29. S.-W. Wang, F. Chen, L. Liang, S. He, Y. Wang, X. Chen, and W. Lu, "A high-performance blue filter for a white-led-based visible light communication system," IEEE wireless communications **22**, 61–67 (2015).
30. T. Kamalakis, "Pyowiot," https://github.com/thomaskamalakis/pyowiot (2022).
31. A. Sivabalan and J. John, "Modeling and simulation of indoor optical wireless channels: a review," in *TENCON 2003. Conference on Convergent Technologies for Asia-Pacific Region,* vol. 3 (IEEE, 2003), pp. 1082–1085.
32. R. Boluda-Ruiz, P. Rico-Pinazo, B. Castillo-Vázquez, A. García-Zambrana, and K. Qaraqe, "Impulse response modeling of underwater optical scattering channels for wireless communication," IEEE Photonics J. **12**, 1–14 (2020).
33. M. B. Rahaim, J. Morrison, and T. D. Little, "Beam control for indoor fso and dynamic dual-use vlc lighting systems," J. Commun. Inf. Networks **2**, 11–27 (2017).